nature communications

Article

https://doi.org/10.1038/s41467-026-69387-z

Intraplanar percolation and interplanar bridge enables layered matrix for high-performance negative electrode

Received: 17 March 2025

Accepted: 1 February 2026

Published online: 10 February 2026

Check for updates

Siyuan Ma[1,2,6], Wengang Yan[1,2,6], Shaobo Wu[1,2], Xinge Sun[1,2], Yu Dong[1,2], Xinyu Zhu[1,2], Tao Liu[1,2], Yizhi Zhai[1,2], Lai Chen[1,2], Qing Huang[1,2], Meng Wang[2], Yibiao Guan[3], Wang Hay Kan[4], Yuefeng Su[1,2,5] ✉, Feng Wu[1,2] & Ning Li[1,2,5] ✉

The rapid advancement of modern technologies has increasingly heightened the demand for rechargeable batteries that exhibit higher energy density, faster charging capabilities, and longer cycle life. However, current battery materials are unable to meet these requirements due to their inherent structural limitations. Therefore, it is essential to design a multifunctional battery material structure, including ample Li^+ storage, rapid Li^+ diffusion, and enhanced structural stability. Here we show a layered structure featuring interplanar bridges and intraplanar percolation that integrates the advantages of currently commercialized mainstream battery material structures. It enables efficient ion transport and structural stability, delivering high capacity/rate capability, long cycle life, and nearly zero-strain structural evolution over a wide temperature range. The versatility of such structural design principle is further confirmed by other materials, and this general principle of discovering and designing advanced battery materials should accelerate the development of next-generation rechargeable batteries.

Lithium-ion batteries (LIBs) have shown significant success in powering portable electronic devices, renewable energy storage, and electric vehicles. However, numerous technical progress generate versatile demands for the LIBs, which current batteries cannot meet[1–4]. The ultimate pursuit of future rechargeable batteries is high energy/power density, long cycle life, all-climate durability, and high safety. Currently, conversion-type and alloy-type battery materials with huge volume change and poor cycle life are difficult to meet these requirements, while the intercalation-type materials maintain relative stability with comparable volume change during lithiation/delithiation, showing great potential to develop versatile LIBs for future demands[5–7].

Generally, two-dimensional (2D) layered materials in Fig. 1a, have garnered significant commercial interest owing to their notable advantages, including large reversible theoretical capacity and 2D transport pathways, such as graphite negative electrodes, layered $LiNi_xMn_yCo_zO_2$ positive electrodes, and $LiCoO_2$. However, the 2D transport pathways in layered matrix are still hard to afford rapid Li^+ diffusion, especially for low-temperature output, and their anisotropic volume changes would also lead to stress accumulation and poor cycling performance[8–11]. On the other hand, the spinel structure in Fig. 1b, with three-dimensional (3D) Li^+ diffusion channels, significantly improves the Li^+ diffusion coefficient, resulting in enhanced rate performance. However, excess interplane bridges between adjacent layers occupy too many sites for Li^+ intercalation, resulting in the low theoretical capacity for high-energy applications. Among various reported electrode materials, $Li_{1+y}[Li_{1/3}Ti_{5/3}]O_4$ $(0 \le y \le 1)$ stands out as a

[1]School of Materials Science and Engineering, Beijing Key Laboratory of Environmental Science and Engineering, Beijing Institute of Technology, Beijing, PR China. [2]Beijing Institute of Technology Chongqing Innovation Center, Chongqing, PR China. [3]National Key Laboratory of Renewable Energy Grid-Integration (China Electric Power Research Institute), Haidian District, Beijing, China. [4]Spallation Neutron Source Science Center, Dongguan, Guangdong, PR China. [5]Beijing Institute of Technology Zhuhai Campus, Zhuhai, PR China. [6]These authors contributed equally: Siyuan Ma, Wengang Yan.
✉e-mail: suyuefeng@bit.edu.cn; ningli@bit.edu.cn

https://doi.org/10.1038/s41467-026-69387-z

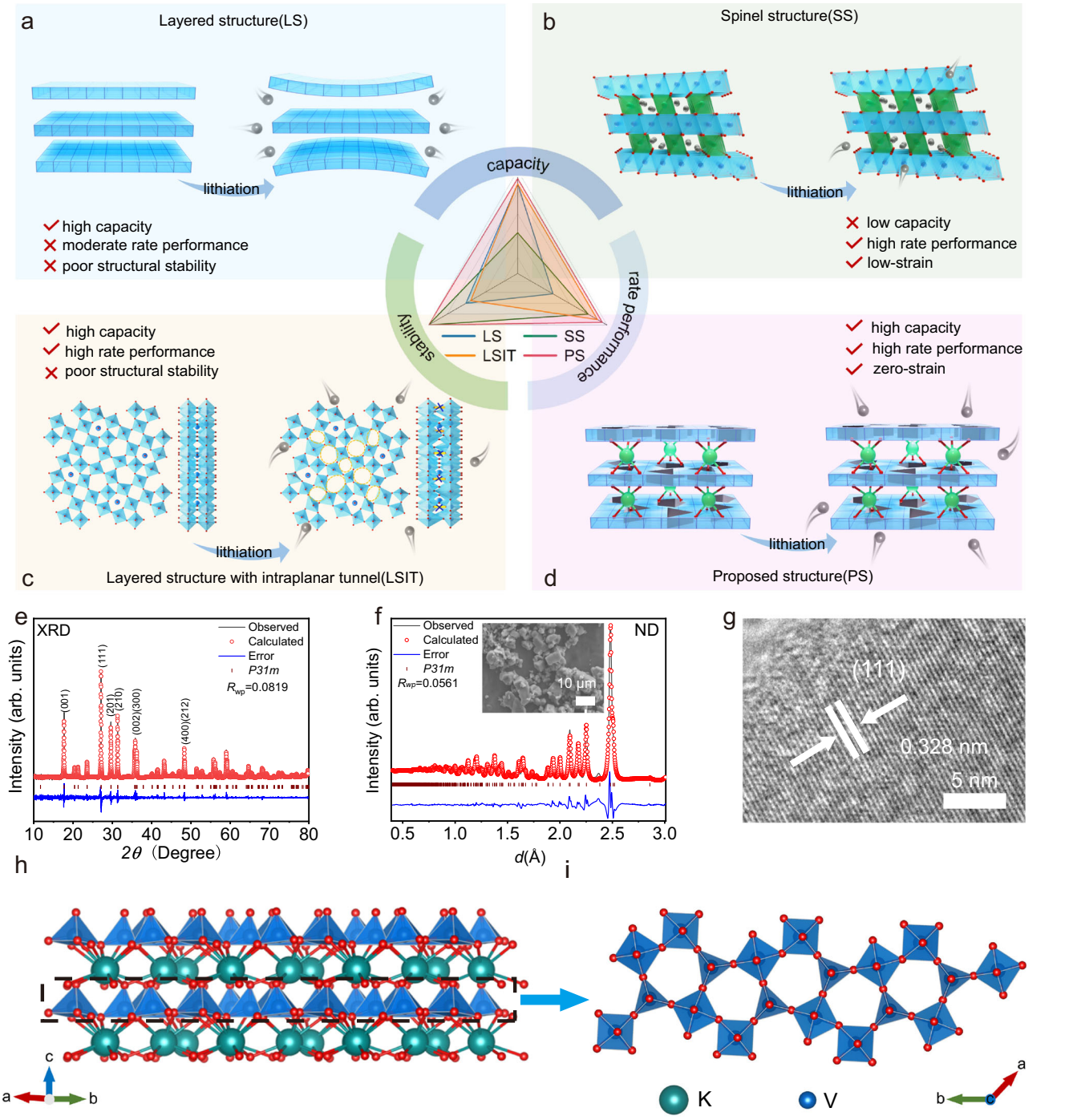

Fig. 1 | The proposed strategy to design advanced battery materials. Layered structure (**a**) Spinel structure (**b**) Layer-like structure (**c**) and the proposed structure (**d**). Note: Li (gray), active TM layer (blue) and inactive ions (green). Physical characterizations of KVO: **e** XRD pattern with Rietveld refinement. **f** ND pattern with Rietveld refinement (inset: FESEM image). **g** HRTEM image of KVO. **h, i** Schematic crystal structure of KVO.

representative of spinel structure with a lattice expansion of less than 0.2% for long-cycle-life negative electrode materials, while the spinel structure also endows the material with low theoretical capacity (175 mAh g^{-1}) and rather high operating potential of approximately 1.55 V vs. Li^+/Li, both of these factors significantly constrain its energy density[12,13].

Recently, plenty of efforts have been devoted to developing high-capacity and fast-charging negative electrode materials for LIBs. To realize this goal, researchers focus on searching for materials that maintain the layered structure with high capacity while constructing tunnels along the layers to realize fast ionic transportation by intralayer percolation. In recent years, the shear ReO_3 structures (e.g., $Ti_2Nb_{10}O_{29}$, $Nb_{14}W_3O_{44}$, $Nb_{16}W_5O_{55}$, and $Ni_2Nb_{34}O_{87}$) and tungsten bronze structures (e.g., $Nb_{18}W_{16}O_{93}$ and T−Nb_2O_5) as shown in Fig. 1c, have garnered considerable attention in the field of fast-charging negative electrode materials, and such structures not only facilitate rapid Li^+ diffusivity, but also show enhanced intercalation-pseudocapacitive behavior[14–18]. Despite their advantages, neither the shear ReO_3 structure nor the tungsten bronze structure demonstrate sufficient stability after deep charge/discharge cycling, and the huge

cell volume expansion and phase transitions during Li^+ insertion would result in a gradual accumulation of lattice strain, ultimately leading to attenuation during prolonged cycling[19–21]. Consequently, to develop future negative electrode materials for high-energy, fast-charging and long-cycling LIBs, it is essential to design material structures with versatile functions: vast Li^+ storage sites, fast Li^+ diffusivity and stable framework under deep and long cycling.

In this work, to develop high-capacity, fast-charging and long-cycling battery materials, we propose a strategy utilizing a layered structure with interplanar bridge and intraplanar percolation by combining the merits of the above-mentioned material structures as shown in Fig. 1d. In such structure, the active transition metal (TM) layer contains numerous tunnels that promote intraplanar percolation. Additionally, the proper amounts of inactive ions with large radius between the layers not only effectively expand the interlayer spacing without consuming many Li^+ intercalating sites, but also firmly suppress the expansion of the active TM layers, even endowing the material with zero-strain characteristic[22–24]. After material structural searching and evaluation, $K_3V_5O_{14}$(KVO), a low-cost vanadium-based compound, was selected to verify our design strategy. In KVO, the edge-shared VO_4 tetrahedrons and VO_5 pentahedrons consist of the active TM layers with multiple open tunnels for Li^+ percolation and dual redox couples (V^{5+}/V^{3+}), while the KO_{10} polyhedrons serve as pins to rivet these active TM layers, which not only expand interlayer spacing, but also attribute to this wide 3D network with robust mechanical stability. Meanwhile, KVO with the low cost of potassium (K) and vanadium (V) elements renders it a cost-effective option for large-scale applications. The as-prepared KVO compound displays a high capacity of 377 mAh g^{-1}, enhanced rate performance (approximately 146 mAh g^{-1} at 10 C) and cyclability retaining 88.3% capacity after 19,000 cycles. In-situ X-ray diffraction (XRD), in-situ/ex-situ transmission electron microscopy (TEM), synchrotron radiation based X-ray absorption spectroscopy (XAS), neutron diffraction (ND), time of flight secondary ion mass spectrometry (TOF-SIMS) and density functional theory (DFT) calculations unveil that the prolonged cycling stability is attributed to the zero-strain structural evolution of KVO, and the high rate performance can be explained by the 3D conduction networks for Li^+ and robust LiF-enriched solid electrolyte interphase (SEI) of KVO. This strategy to develop negative electrode materials is also further verified by other materials and sheds light on the development of fast-charging, long-life negative electrode materials for future LIBs.

Results

Crystal structure and characteristics

The KVO material is prepared by the simple ball milling process, and the corresponding XRD and ND patterns of the as-prepared KVO are depicted in Fig. 1e, f and Supplementary Tables 1 and 2. Rietveld refinement shows that all Bragg diffraction peaks can be well indexed to an orthorhombic system with a space group of P31m (JCPDS card No. 14-555). The field emission scanning electron microscopy (FESEM) images in the inset of Fig. 1f reveal that KVO presents as micron-sized particles ranging from 1 to 20 μm. HRTEM image in Fig. 1g confirms well-defined (111) planes with an interspacing of 0.328 nm, and TEM with energy-dispersive X-ray spectroscopy (EDS) (Supplementary Fig. 1) shows the uniform distribution of K, V, and O in the KVO sample. The crystal structure of KVO is further depicted in Fig. 1h, i. The VO_4 tetrahedrons and VO_5 square pyramids collectively form $(V_5O_{14})^{3-}$ TM slabs, and the top view shows these TM slabs contain abundant pentagonal tunnels, which would be favorable for Li^+ percolation along the slabs. Meanwhile, all these TM layers are stacked along the *c* axis direction, and the K^+ with neighboring O to form KO_{10} polyhedrons, serve as bridges to rivet the adjacent TM slabs with A-B-A stacking. Thus, we successfully synthesized the KVO layered material, and the TM slabs with intraplanar percolating ability and KO_{10} with robust interplanar bridge in such layered material generate abundant open tunnels for 3D Li^+ transportation and vast sites for Li^+ intercalation and volume accommodation. Furthermore, KVO exhibits a remarkably small band gap of 2.17 eV by UV–vis absorption test (Supplementary Figs. 2 and 3), demonstrating much higher electronic conductivity of 6.34×10^{-8} S cm^{-1} than $Li_4Ti_5O_{12}$ materials[25].

Electrochemical advantages of the as-prepared KVO

To explore the electrochemical advantages of the as-prepared KVO material, it was fabricated as the negative electrode to be charged/discharged in the half cell and full cell as shown in Fig. 2. Supplementary Fig. 4 displays the initial four discharge/charge curves of KVO in half cell at 0.1 C (1 C = 450 mA g^{-1}), ranging from 0.2 to 3.0 V at 30 °C. In the first discharge cycles, the capacity of KVO exhibited more than 700 mA h g^{-1} [26–28].The origin for the extra capacity can be attributed to 1) the formation of the SEI, resulting from electrolyte decomposition above 0.4 V vs. Li^+/Li, 2) the obvious Li^+-storage by conductive carbon (Super P) at low potentials, and 3) intercalation-type negative electrode materials that the inserted Li^+ ions during the first lithiation cannot be totally extracted. (Supplementary Figs. 5 and 7) When we use the active mass up to 90 %, the initial coulomb efficiency and charge capacity becomes more reasonable. (Fig. 2a) After initial lithiation, the KVO negative electrode presents similar discharge/charge curves in subsequent cycling, suggesting a highly reverside-lithiation pr/delithiation process. Figure 2b shows that the KVO sample displays a reversible capacity of 377 mAh g^{-1} (84% of its theoretical capacity, which is based on the results of theoretical calculations (Supplementary Figs. 8 and 9 and Supplementary Data 1)) at 0.1 C, which is 2.5 times higher than that of commercial $Li_4Ti_5O_{12}$, and higher than that of commercial graphite. Meanwhile, it can also be clearly seen that KVO operates at a quite suitable working potential of ~1.45 V vs. Li^+/Li, which is notably higher than the threshold for lithium dendrite formation (Supplementary Figs. 10 and 11 and Supplementary Table 3) and lower than 1.55 V vs. Li^+/Li of the renowned $Li_4Ti_5O_{12}$[29,30]. The low-voltage operation of KVO primarily originates from diminished crystal field stabilization in tetrahedral VO_4 units, augmented by isotropic 3D ion diffusion and zero-strain lattice accommodation[31–34]. Supplementary Fig. 12 demonstrates high rate performance, delivering reversible capacities of 298, 263, 233, 192, and 147 mAh g^{-1} at 0.5, 1, 2, 5, and 10 C, respectively. At 10 C, the capacity of the KVO material maintains almost half of that at 0.5 C. Under the identical 10 C condition, the graphite negative electrode exhibits a lower capacity retention rate of only 6% relative to its own 0.5 C capacity. (Supplementary Figs. 13 and 14).

The cycling performance is further characterized at different C rates. Notably, the KVO negative electrode demonstrates a high-capacity retention of 90.2 % over 500 cycles at 1 C in Fig. 2c. At 5 C, it remains a capacity retention of nearly 100.0 % without capacity attenuation over 2000 cycles in Fig. 2d. At a high rate of 10 C, it maintains 95.0 % capacity retention over 10,000 cycles. Even after 19,000 cycles, the KVO negative electrode still exhibits capacity retention of 88.3 % in Fig. 2e. The cycling stability of KVO in this study is at a relatively high level in the field of electrochemical energy storage materials. (Fig. 2f and Supplementary Table 4). To further validate the advantages of KVO as a negative electrode, we narrowed the voltage range to 0.1 V – 2 V. The average operating voltage within this range was ~0.78 V vs. Li^+/Li, the material demonstrates promising electrochemical performance. (Supplementary Fig. 15)

To further investigate the electrochemical merits of the KVO negative electrode material, it was cycled at both high temperature (60 °C) and low temperature (−10 °C) in Fig. 2g, h. The capacity and capacity retention of KVO at different C rates show slight enhancement at 60 °C. It shows a high reversible capacity of 396 mAh g^{-1} at 0.1 C (Supplementary Fig. 16), slightly higher than that at 30 °C. And it also maintains capacities of 348, 317, 282, 224, and 175 mAh g^{-1} at 0.5 C, 1 C, 2 C, 5 C, and 10 C, respectively (inset of Fig. 2g). More importantly, the

https://doi.org/10.1038/s41467-026-69387-z

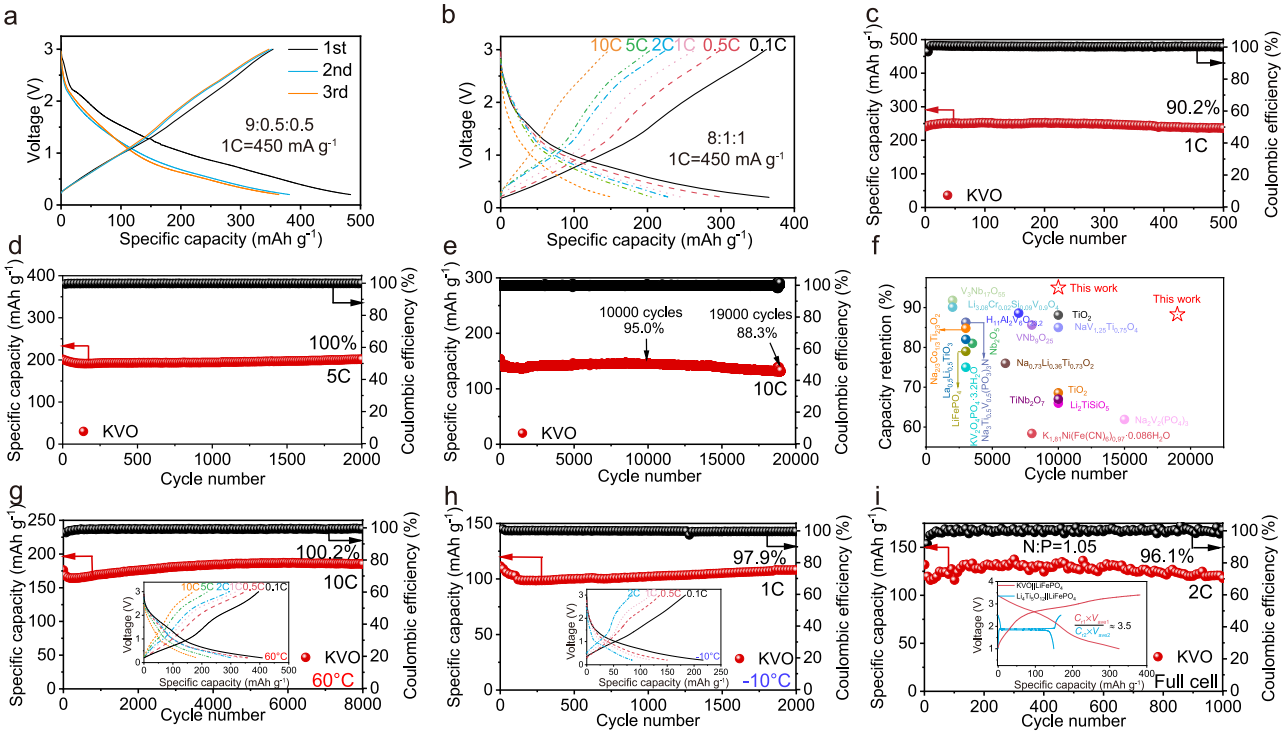

Fig. 2 | Electrochemical performance of KVO half and full cells. (1 C = 450 mA g^{-1} for KVO). a Discharge/charge profiles of Li | |KVO cell at 0.1 C for initial three cycles within 0.2–3.0 V at 30 °C (90%KVO: 5%Super P: 5%PVDF (polyvinylidene fluoride)). **b** Discharge/charge profiles of Li | |KVO half cell from 0.1 C to 10 C within 0.2 – 3.0 V at 30 °C. (80%KVO: 10%Super P: 10%PVDF) (**c**–**e**) Cyclability of Li | |KVO half cell after rate test at 30 °C. (80%KVO: 10%Super P: 10%PVDF) **f** The cycling stability of KVO is compared with that of other well-known long-life electrochemical energy-storage materials documented in prior studies (Refer to Supplementary Table 4). **g** Cyclability at 10 C over 8000 cycles at 60 °C (inset: Discharge/charge profiles from 0.1 C to 10 C at 60 °C, 80%KVO: 10%Super P: 10%PVDF). **h** Cyclability at 1 C over 2000 cycles at −10 °C (inset: Discharge/charge profiles from 0.1 C to 2 C at −10 °C, 80%KVO: 10%Super P: 10%PVDF). **i** Cyclability of KVO | |$LiFePO_4$ full cell at 2 C under 30 °C over 1000 cycles, N/P ratio is 1.05, and the capacity is calculated based on mass of KVO (inset: Comparison of KVO | |$LiFePO_4$ with $Li_4Ti_5O_{12}$ | |$LiFePO_4$ in terms of specific capacity, operating voltage, and specific energy).

KVO sample yields a capacity retention of 100.2 % after 8000 cycles at 10 C in Fig. 2g. In stark contrast, $Li_4Ti_5O_{12}$ exhibits a retention of only 20.9 % after 500 cycles at 5 C, and commercial graphite particles exhibit a retention of only 36.7 % after 1000 cycles at 10 C[16,25]. Meanwhile, when cycled at −10 °C, KVO demonstrates a capacity of 184 mAh g^{-1} at 0.1 C (Supplementary Fig. 17) and a rate performance of 84 mAh g^{-1} at 2 C (inset of Fig. 2h). Additionally, it shows capacity retention of 97.9 % at 2 C over 2000 cycles (Fig. 2h). To assess the commercialization potential of KVO, KVO | |$LiFePO_4$ full cell was assembled. It is worth noting that the KVO | |$LiFePO_4$ full cell exhibits a large reversible capacity (326 mAh g^{-1}) at a current density of 0.1 C and average operating voltage of 2.65 V in inset of Fig. 2i. And its specific energy (on an active material mass basis) is 3.5 times that of $Li_4Ti_5O_{12}$ | |$LiFePO_4$. Figure 2i shows that KVO maintains a capacity retention of 96.1 % after 1000 cycles at 2 C. Meanwhile, the KVO | |$LiFePO_4$ interdigital battery in Supplementary Fig. 18 also exhibits high capacity and prolonged cycling stability. The negligible voltage polarization changes observed in the long-term cycling curves of half cell and full cell at different rates (Supplementary Fig. 19) indicate that KVO has high structural integrity. It should be mentioned that the slight capacity increases of the Li | |KVO half cells during the electrochemical reaction can be explained by the continuous KVO activation. (Supplementary Fig. 20 and Supplementary Table 5)[35,36] Therefore, the electrochemical characterizations demonstrate that the KVO material shows a great potential to stand out as a practical negative electrode material with high capacity, long lifespan, fast-charging capability and all-climate operation for wide-range applications such as electric vehicles, large-scale energy storage and so on.

Reversible bulk chemical evolution and stable surface chemistry

To better understand the electrochemical performance of KVO, we probe the bulk chemical evolution in KVO during cycling by hard XAS. The samples for detailed tests were selected according to the Cyclic Voltammetry (CV) curves in Supplementary Fig. 21. There are two characteristic regions in the spectra: the pre-edge peaks in the range 5465–5470 eV, and main peaks at about 5484 eV. The oxidation state of the V is known to be sensitive to the intensity ratio between the pre-edge and main peaks (referred to as P/M hereafter)[1,37,38]. It can be seen that the valence state of V is +5 at pristine state in Fig. 3a, and then the P/M value decreases from 0.88 to 0.77 when KVO is discharged to 0.6 V, and the P/M value further decreases to 0.46 when discharged to 0.2 V, which is significantly lower than the reference value of 0.70 for V^{4+}. This observation indicates the a two-electron transfer process from V^{5+} to V^{3+} in the KVO sample. Conversely, during charging, the P/M value gradually increases and nearly approaches to the original state at the end of charge (Fig. 3b). To investigate the chemical evolution of the near surface, soft XAS were collected at total fluorescence yield (TFY) mode with a detection depth of 50 ~ 100 nm. Figure 3c shows the V L-edge spectra of the pristine KVO sample exhibit two main peaks at 517.5 eV for V-2$p_{3/2}$ and 524.9 eV for V-2$p_{1/2}$, respectively, which can be used as V^{5+} reference. When the electrode is gradually discharged to 0.2 V, the two main peaks gradually drift to lower energy levels, and interestingly, the intensities of their shoulder peaks gradually increase. The comparison between the sample at 0.2 V and standard reference samples indicates the coexistence of V^{4+} and V^{3+} at the end of discharge. Conversely, during charging, the V L-edge spectra progressively recover and return to their pristine state upon

https://doi.org/10.1038/s41467-026-69387-z

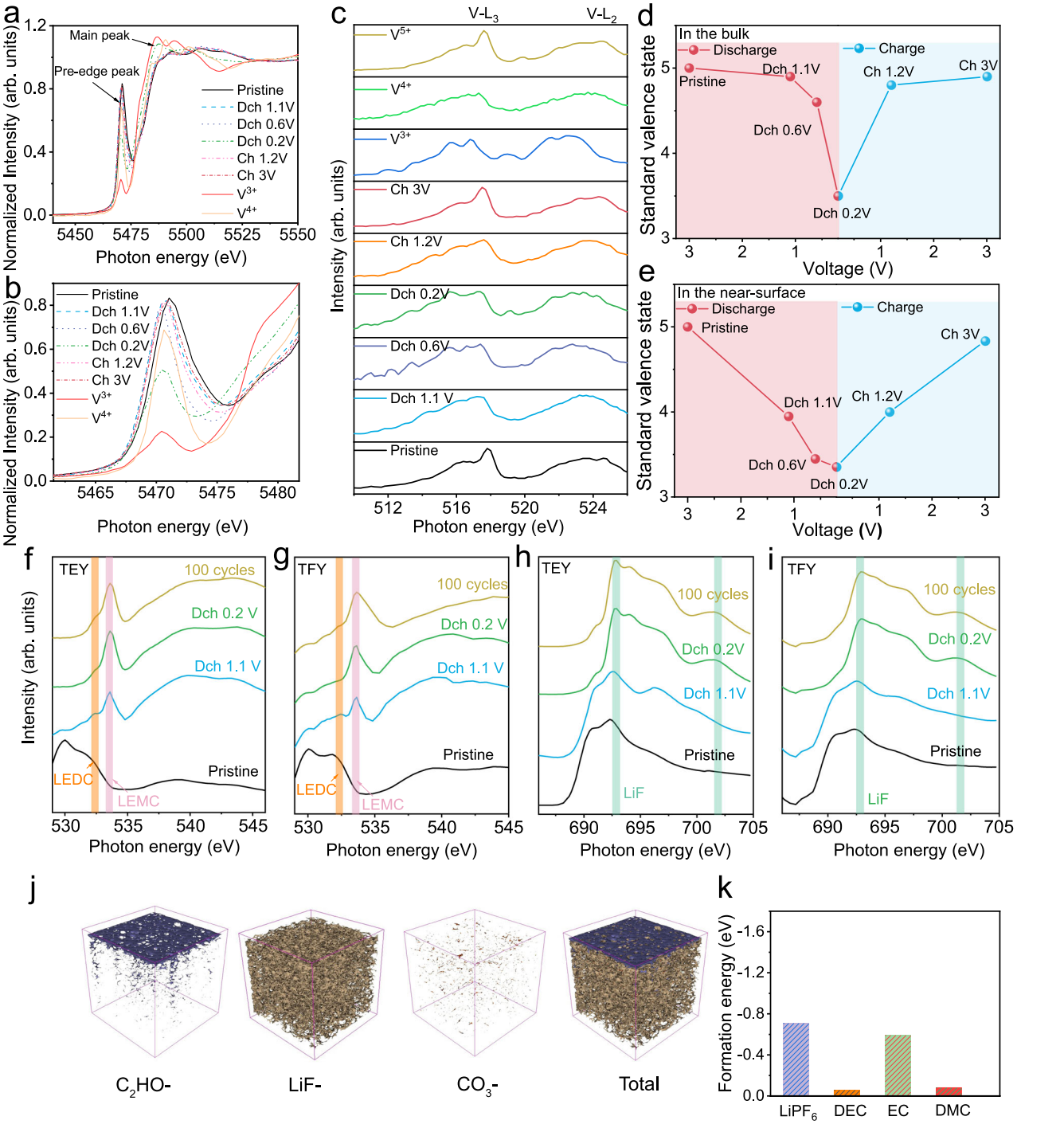

Fig. 3 | Bulk and surface chemical evolution of KVO. a, **b** XANES of V K-edge. **c** V L-edge soft XAS TFY spectra. **d**, **e** Valence changes of the near-surface and bulk phases of V measured at different discharge/charge states. **f** O K-edge soft XAS TEY spectra. **g** O K-edge soft XAS TFY spectra. **h** F K-edge soft XAS TEY spectra. **i** F K-edge soft XAS TFY spectra. **j** The 3D views of LiF-, CO_3– and C_2HO- in the TOF-SIMS sputtered volumes of SEI layers for KVO electrodes after 100 cycles under conditions of 1 C at 30 °C. **k** The affinity energy and desolvation barrier of various electrolyte components for KVO.

charging to 3 V. The ex-situ X-ray Photoelectron Spectroscopy (XPS) characterization also confirms this surface evolution in Supplementary Fig. 22. The valence state changes of V in the surface (50 ~ 100 nm) and the bulk are further illustrated clearly in Fig. 3d, e. It is worth noting that V can be almost recovered to +5 during the charge process in both bulk and surface, indicating the highly reversible V redox, the slight discrepancy from the original state is attributed to incomplete extraction of trace Li^+ ions during the initial cycle[39,40]. At the same time, V undergoes a two-electron transfer from V^{5+} to V^{3+} in both bulk and surface, while there is slight charge heterogeneity from bulk to surface as well. Ex-situ Raman spectroscopy (Supplementary Fig. 23) demonstrates the highly reversible structural behavior of KVO, with characteristic V–O bending vibrations at 930 and 962 cm^{-1} showing no peak shifts or new phases, consistent with its zero-strain characteristic[41–45]. However, a slight attenuation in restored Raman intensity after delithiation suggests minor irreversibility. Electron

Energy Loss Spectroscopy (EELS) analysis (Supplementary Fig. 24) reveals slight surface oxygen defects, where Li^+ ions become trapped during initial lithiation through stabilization by defect sites and local reduction of V^{5+} to V^{4+} (Supplementary Table 6, Supplementary Fig. 25 and Supplementary Data 2)[41,46,47]. The synergistic effect of shallow Li trapping and zero-strain lattice confinement maintains bulk V^{5+} stability while accommodating surface reduction, preventing bulk degradation and enabling favorable structural integrity and cycling stability[48–51].

The SEI is crucially important for the cycling performance of negative electrode materials, and to elucidate the chemical evolution of SEI in the KVO material, the O and F K-edge soft XAS spectra at both total electron yield (TEY) and TFY modes were collected at different charge and discharge states[52]. Figure 3f, g show the TEY and TFY data for O K-edge XAS spectra, and at pristine state, only the lattice oxygen signal can be seen in both modes. When the electrode is discharged to 1.1 V, a slight oxygen signal of SEI emerges at 534 eV at both TEY and TFY modes, and these signals are resembled those of organic carbonates such as LEMC (lithium ethylene mono-carbonate), LEDC (lithium ethylene di-carbonate) (Supplementary Figs. 26 and 27). The peak intensities for SEI at both TEY and TFY modes become more obvious when the electrode is further discharged to 0.2 V, indicating a significant oxygen compound formation in SEI. The intensity for SEI remains stable even after 100 cycles, further suggesting the stable oxygen compounds form in SEI after the initial cycle. Meanwhile, the peak intensity for oxygen compounds of SEI at TFY mode is much lower than that at TEY mode, possibly due to the enrichment of combinates in the surface layer of the electrode. Additionally, F K-edge soft XAS spectra at TEY and TFY modes are depicted in Fig. 3h, i and Supplementary Fig. 28, respectively. There is only a signal for PVDF binder at pristine state at both modes, and after discharging to 1.1 V, LiF starts to emerge. The LiF becomes a dominant compound at 0.2 V discharge and remains quite stable even after 100 cycles. There are no obvious spectral differences between the TFY and TEY data, inferring the LiF-rich SEI formation in the KVO sample.

To further investigate the structure and chemical composition of the SEI, TOF-SIMS analysis was conducted on the KVO sample after 100 cycles. Supplementary Fig. 29 displays the depth analysis curve of the KVO electrode, revealing characteristic ion fragments of LiF- and C_2HO-, which confirm the presence of LiF and organic carbonates in SEI. As the sputtering time increases, the LiF content gradually increases while the organic composition sharply decreases, as depicted in Fig. 3j. Hence, combined with the soft XAS data, it can be found that SEI on the KVO electrode exhibits a clear bilayer structure, comprising an external organic layer and an internal inorganic layer (markedly enriched in LiF). This result is well consistent with the TEM results in Supplementary Fig. 30. Therefore, the stable LiF-enriched SEI formed in the KVO material is believed to play a crucial role in enhancing the Li^+ diffusivity and long cycling performance. To determine whether LiF enrichment was specific to KVO or inherent to the vanadate framework, we performed comparative TOF-SIMS studies on isostructural $K_2MgV_2O_7$ (Supplementary Fig. 31). Crucially, this $K_2MgV_2O_7$ exhibited the same pronounced LiF dominance in its SEI. DFT calculations uncovered a surface-selective reaction pathway driving $LiPF_6$ decomposition: Fluorine exhibits significantly higher electronegativity than oxygen, enabling stronger ionic-covalent hybrid bonds with electropositive vanadium sites. From a thermodynamic perspective, this is conducive to the selective adsorption of $LiPF_6$ on the electrode surface. Compared with common electrolyte decomposition products such as EC (−0.59 eV) or DEC (−0.056 eV), the calculated adsorption energy (−0.708 eV) is significantly higher. When $LiPF_6$ approaches the KVO surface, PF_6^- anions undergo site-specific chemisorption (Fig. 3k, Supplementary Fig. 32, Supplementary Table 7 and Supplementary Data 3). The LiF-rich SEI originates from the inherent fluorophilicity of exposed vanadium centers in layered vanadates, where strong V–F bonding drives preferential PF_6^- decomposition and localized LiF precipitation. (Supplementary Figs. 33 and 34 and Supplementary Data 4) This mechanism, which is generalizable across vanadate frameworks, represents an intrinsic interfacial property that complements the structural advantages of KVO.

Zero-Strain structural evolution at wide-temperature cycling

The crystal-structure evolution of KVO during charge and discharge was explored through in-situ XRD characterization[15]. After the initial activation in Supplementary Fig. 35, the in-situ XRD patterns of the subsequent two cycles at 0.2 °C and 30 °C are illustrated in Fig. 4a. It can be seen that all patterns nearly show no change upon cycling. The enlarged view of patterns in Supplementary Fig. 36 shows that the (001) and (111) peaks slightly shift to higher 2θ angles during the first charge, and then drift back to their original positions during the second discharge, and reversibly evolve after cycling as shown in Fig. 4a. The (001) and (111) peaks change in P31m structure indicate three possible Li^+ occupation sites, 1a, 3c(1), and 3c(2) in KVO (Fig. 5d and Supplementary Fig. 51), which will be discussed later. Meanwhile, the intensities of all diffraction peaks slightly decrease and then almost fully recover during cycling. Such highly reversible single-phase evolution serves as strong evidence to rather favorable structural reversibility and stability of KVO during the repeated charging and discharging process. Furthermore, all the precise lattice parameters of KVO during cycling are calculated by Rietveld refinement as shown in Fig. 4b and Supplementary Fig. 37. All the lattice parameters a, c and V exhibit high reversibility and zero-strain characteristic with maximal variations of approximately 0.11 %.

To further explore the structural merits of the as-prepared materials, an additional in-situ XRD test was conducted at 60 °C in Fig. 4c and Supplementary Fig. 38. The directions of peak shifts remain consistent with those observed at 30 °C, while the peak drift degree is slightly larger than that at 30 °C. Rietveld refinement of the in-situ XRD patterns at 60 °C shows the maximum change in V-value slightly increases to 0.36 % in Fig. 4d and Supplementary Fig. 39. The increment is evidently attributed to the larger reversible Li^+-storage capacity at 60 °C (Supplementary Fig. 16). Notably, the zero-strain characteristic persists at 60 °C for the KVO material. This desirable trait of zero-strain at various temperatures undoubtedly contributes to its prolonged cycling stability across a wide-temperature range, particularly at 60 °C. This is one of the lower percentages observed in Li^+ storage materials (Fig. 4e and Supplementary Table 8).

In-situ TEM was employed to further investigate the microstructural and morphological evolution of KVO during lithiation[53,54]. As highlighted in Fig. 4f, Supplementary Fig. 40 and Supplementary Movie 1, significant movement of strain fringes is observed, originating from Li^+ intercalation in the KVO primary particles, while the microstructure, morphology, and volume of the as-observed KVO particle exhibit negligible change. Ex-situ HRTEM characterization in Supplementary Fig. 41 aligns well with the findings of in-situ TEM, demonstrating unchanged interplane spacing of (201) planes from the pristine to the lithiated and delithiated states. In-situ optical microscopy (Supplementary Fig. 42, Supplementary Movie 2, and Supplementary Movie 3) reveals KVO particles maintain structural integrity with minimal volume change after 100 cycles—in sharp contrast to the severe expansion of graphite—while in-situ XRD (Supplementary Fig. 43) confirms that the zero-strain character of KVO persists even at 0.01 V, demonstrating macroscopic stability. Furthermore, the stress simulation diagrams in KVO multi-particle simulation by COMSOL in Fig. 4g, Supplementary Fig. 44 and Supplementary Movie 4 show the minimal stress and strain reversibility during the initial cycle, and the XRD, FESEM, and TEM characterization in Supplementary Fig. 45 display favorable stability of the KVO electrode after 500 cycles at 5 C. Based on our analysis, we believe that the slight changes in the XRD after the cycle are mainly due to the difference inherent to measuring

https://doi.org/10.1038/s41467-026-69387-z

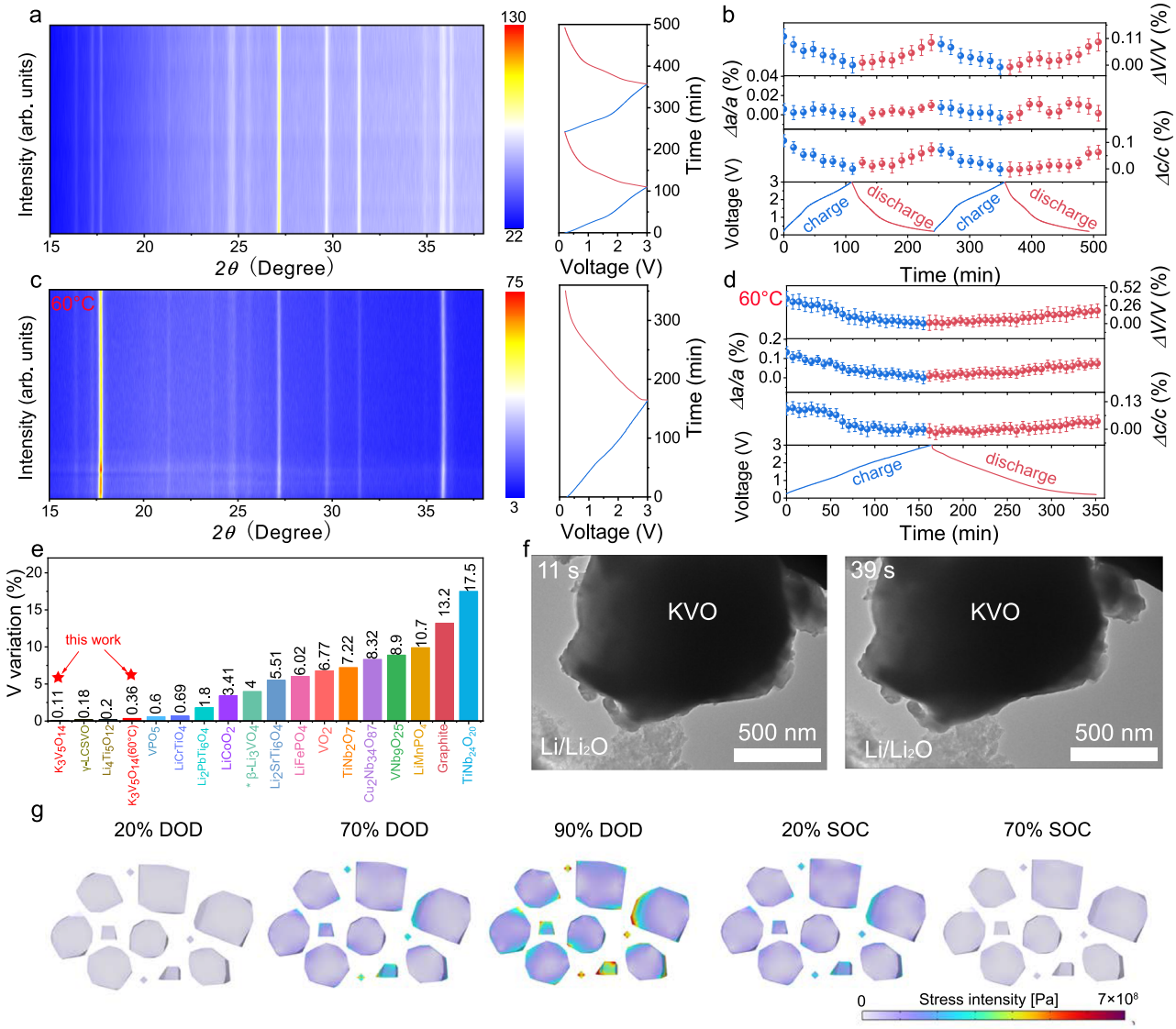

Fig. 4 | Long-term structural evolution of KVO at 30 and 60 °C. a In-situ XRD patterns at 30 °C (two cycle after initial discharge at 0.2 C). **b** Unit-cell-volume variation of KVO with corresponding charge/discharge curves. **c** In-situ XRD patterns of Li | |KVO half cell at 60 °C (one cycle after initial discharge at 0.2 C). **d** Unit-cell volume variation of KVO with corresponding charge/discharge curves at 60 °C (Error bars represent the standard deviation). **e** Comparisons of maximum unit-cell volume change of KVO with Li^+-storage materials previously reported (Refer to Supplementary Table 8). **f** In-situ TEM images of Li^+ intercalation in KVO, driven by applying −3.0 V upon electrode contact. **g** The simulation diagram of stress simulation diagram of KVO with COMSOL software.

electrode sheets versus pure powders, as well as the preferred orientation generated during the rolling process, rather than indicating the presence of phase transformation or structural degradation. (Supplementary Figs. 46 and 48 and Supplementary Table 9) Thus, it is believed that the zero-strain single-phase change at a wide-temperature range, moderate stress, and strain reversibility during cycling enable KVO to sustain over tens of thousands of cycles.

Local structure for zero-strain evolution and electrochemical kinetics

To investigate the origin of the zero-strain characteristic of KVO, we carefully analyze the changes of local structure and chemical bond length through EXAFS and XRD refinement at the lithiated and delithiated states[55–57]. Fig. 5a shows the Fourier transform of V K-edge EXAFS with a selected k-space range of 0 ~ 14 $Å^{-1}$. The R-space curves of V K-edge EXAFS reveal two main peaks corresponding to the first shell for the V–O coordination and the second shell for the V–V coordination, and the horizontal position of the shell indicates the uncorrected bond length, while the intensity the changes in the coordination number (CN) and the Debye-Waller (DW) factor[58]. (Supplementary Table 10)

From the pristine state to 0.2 V discharge, the first shell for the V–O coordination slightly shifts rightward due to the reduction of V^{5+} ions to larger V^{4+}/V^{3+} ions, and then the position of the second shell for interplanar V–V coordination also simultaneously shifts rightward upon 0.2 V discharge. This phenomenon is well consistent with the XRD refinement result, as shown in Fig. 5b and Supplementary Tables 11 and 13, and the lithium intercalation increases the volume of the VO_4 tetrahedron by 1.05 % and the volume of the VO_5 pentahedron by 0.19 %. More interestingly, the KO_{10} polyhedron contracts its volume by 0.42 %, which is possibly attributed to the pillar effect of K buffering the volume expansion of V in redox reactions. During charging, these two shells almost horizontally drift back to their original positions. We performed quantitative EXAFS fitting for both pristine,

https://doi.org/10.1038/s41467-026-69387-z

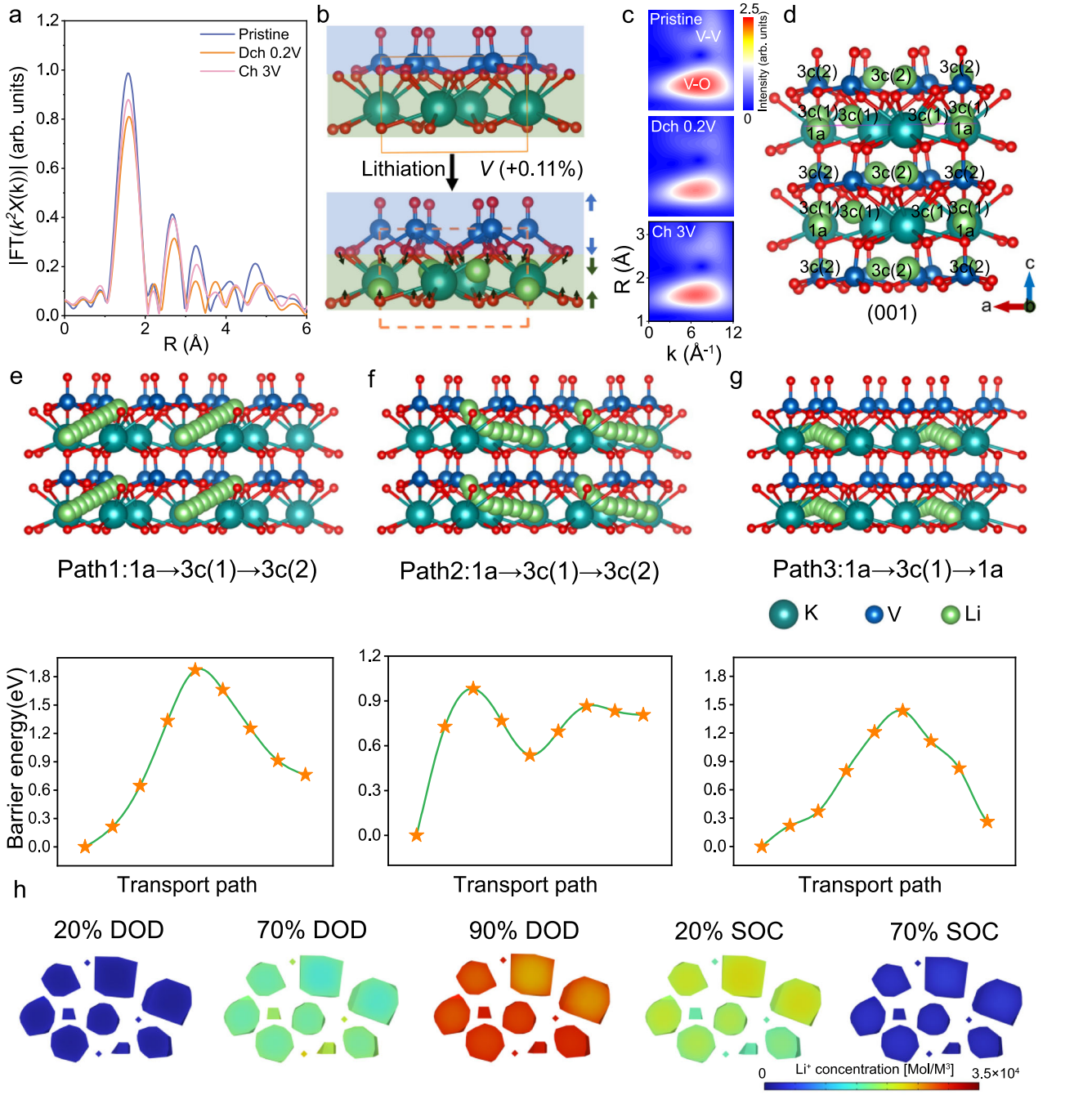

Fig. 5 | Local structural characterization for zero-strain evolution and rapid Li^+ diffusion in KVO. a The corresponding Fourier transforms of V K-edge EXAFS spectra. **b** Movement of ions during lithiation, with K, V, O, and Li depicted in dark green, blue, red, and green, respectively. **c** V K-edge EXAFS WTs during first cycle. **d** Schematic illustration of (001) crystallographic plane. **e**–**g** DFT calculated Li^+-diffusion paths and calculated minimum energy paths by CI-NEB. **h** The simulation diagram of Li^+ concentration distribution diagram of KVO with COMSOL software.

lithiated and delithiated states of KVO. A synergetic variation of parameters is observed: upon discharge, the CN of V–O and V–V decrease slightly from 4.6 to 4.5 and from 2.5 to 2.3, respectively, accompanied by an increase in the DW factor. All parameters recover to values close to the pristine state after charging. This phenomenon depicts a dynamic but perfectly resilient coordination environment undergoing elastic distortion, which is fully consistent with the long-range zero-strain behavior confirmed by our in-situ XRD. (Supplementary Table 10 and Supplementary Figs. 49 and 50) Additionally, the Wavelet-Transformed EXAFS (WT-EXAFS) in Fig. 5c further clearly illustrates that the maximum WT values of the V–O and V–V coordination do not significantly deviate during charging and discharging. Thus, the inactive KO_{10} slabs and active TM slabs in the as-proposed KVO material can mutually compensate each other and effectively buffer the volume change in lattice, demonstrating zero-strain structural change at a wide-temperature range[59].

To gain the origin of the fast charge capability of KVO, the Li^+-transport paths in KVO were further simulated by using DFT (Supplementary Data 5). In-situ XRD in Fig. 4 indicates three possible Li^+ occupation sites, 1a, 3c(1), and 3c(2) in the P31m structured KVO as

shown in Fig. 5d and Supplementary Fig. 51. The formation energy calculation shows Li^+ favorably occupy 1a sites and then the 3c(1) sites (Supplementary Fig. 52). Interestingly, in the optimized crystal model, since the V–O bonds are in a negatively charged state, they are more likely to adsorb Li^+, and the Li^+ are more likely to shift towards the V–O position. For KVO, the maximum inserted Li^+ number is as high as 10 (Supplementary Fig. 9). Within the range of $1 \le x \le 10$, the binding energies of xLi and KVO are both negative, indicating that KVO is suitable for utilization in LIBs. Figure 5e–g illustrate three potential paths for Li^+ transmission: 1a → 3c(1) → 3c(2)(path I), 1a → 3c(1)→3c(2) (path II), and 1a → 3c(1)→1a (path III). Path I illustrates the linear migration of Li^+ along the pathway 1a → 3c(1)→3c(2). The results obtained from the Climb Image - Nudged Elastic Band (CI-NEB) method demonstrate that Path I encounters a relatively high energy barrier of 1.85 eV. The transition state, situated near the 3c(1) sites in Fig. 5e, corresponds to the high energy barrier due to the competitive affinity between V–O and Li–O. Through the transition state, the energy of the V–O bond is reduced to form the Li–O bond. Path II in Fig. 5f represents a special pathway through Li^+ percolation perpendicular to the TM slabs. Li^+ at 1a sites initially migrates to a location adjacent to 3c(1) sites before shifting to 3c(2) sites, featuring a relatively low energy barrier of 0.98 eV. Path III in Fig. 5g shows a bent transport pathway in the inactive KO_{10} slab, which involves Li^+ migration between sites 1a and 3c(1) with a moderate energy barrier of 1.01 eV. It is evident that the barriers of Path II and Path III are notably smaller than that of Path I, and these favorable Li^+ diffusive paths can establish an interconnected 3D large channel for Li^+ transport in KVO, which surely facilitates a rapid Li^+ diffusion. Inductively coupled plasma (ICP) analysis confirming negligible K^+ loss (Supplementary Table 14) combined with DFT calculations revealing a prohibitively high K^+ deintercalation energy (+5.28 eV) versus favorable Li^+ removal (−1.58 eV) (Supplementary Fig. 53, Supplementary Table 15 and Supplementary Data 6) demonstrate that Li^+/K^+ ion exchange is thermodynamically prohibited in KVO. The Galvanostatic intermittent titration technique (GITT) experiments in Supplementary Figs. 54 and 55 and Supplementary Table 16 also indicate a high Li^+ diffusion coefficient (D_{Li+}) of KVO in comparison with other materials. Additionally, COMSOL simulations in Fig. 5h, Supplementary Fig. 56 and Supplementary Movie 5 visualize the Li^+ concentration distribution diagram in KVO multi-particles, and the 3D channels enable that the Li^+ concentration distribution is relatively uniform with small gradient and almost non-disparity from bulk to surface in particles during discharge and charge. Therefore, the theoretical calculations combined with the experiment results elucidate the 3D pathway for Li^+ diffusion, which is attributed to the rapid Li^+ diffusion and fast-charging capability of KVO.

Universality of the strategy to discover advanced zero-strain battery materials

The proposed strategy to search a high capacity, high-rate and long-cycling zero-strain negative electrode material is successfully demonstrated by the KVO sample. The KVO sample displays a layered structure with intraplanar percolation and interplanar bridge. To explore the universality of this proposed strategy, we further search and investigate some other compounds with similar layered structures in Fig. 6. Figure 6a shows the XRD patterns of the $K_2VP_2O_8$ material prepared via a simple ball milling method. Rietveld refinement reveals that all Bragg diffraction peaks can be successfully indexed to a tetragonal system with the space group P-421m (JCPDS card No. 40-283). (Supplementary Table 17) The schematic diagram of the crystal structure for $K_2VP_2O_8$ is illustrated in Fig. 6b. Similar to KVO, the VO_5 pentahedrons and PO_4 tetrahedrons interconnect to form tunnels in the TM slab, and KO_8 serves as an inactive layer to pin-bridge the adjacent TM slabs. As anticipated, $K_2VP_2O_8$ exhibits reversible capacity (306 mAh g^{-1} at 0.1 C), rate capability (133 mAh g^{-1} at 10 C) and cyclability, with a capacity retention of 93.8 % at 10 C over 1200 cycles (Fig. 6c and Supplementary Fig. 57). More importantly, Fig. 6d illustrates in-situ XRD patterns at the initial two cycles at 0.3 C at 0.01–3.0 V. It is evident that nearly all peaks display negligible shift during the repeated Li^+ insertion/extraction process. Additionally, Fig. 6e shows the XRD spectra of another compound, $K_2MgV_2O_7$ with a crystalline space group of P42/mnm. (Supplementary Table 18) The schematic diagram in Fig. 6f indicates that the MgO_4 tetrahedrons and VO_4 tetrahedrons interconnect to form tunnels in the TM slab, and KO_8 serves as an inactive layer to pin-bridge the adjacent TM slabs. Similarly, $K_2MgV_2O_7$ delivers a capacity of 339 mAh g^{-1} at 0.1 C, rate capability of 126 mAh g^{-1} at 10 C, and a capacity retention of 95.2% after 2000 cycles at 10 C. (Fig. 6g and Supplementary Fig. 58). As anticipated, the $K_2MgV_2O_7$ sample also exhibits zero-strain structural evolution during cycling as shown in Fig. 6h. Similarly, we have synthesized phase-pure $Rb_3V_5O_{14}$ via solid-state reaction, confirmed by XRD, SEM, and TEM without impurities (Fig. 6i, Supplementary Fig. 59a–c and Supplementary Table 19), and demonstrated electrochemical performance (Supplementary Fig. 59d–f): rate capability of 107 mAh g^{-1} at 5 C, long-term cycling stability with 87.1% capacity retention after 1000 cycles at 5 C, and near zero-strain behavior (Fig. 6j).Thus, our study demonstrates a general principle for searching and designing materials with zero-strain, high capacity, long-cycling and fast charging capabilities. This structural innovation differs significantly from conventional doping. (Supplementary Table 20) These layered structure materials are essential to maintain active TM layers with abundant open tunnels that facilitate intraplanar percolation, and also rivet appropriate amount of inactive ions between TM slabs to form inactive layers with vast interlayer space for Li^+ storage and diffusion, which are also mainly used to buffer the expansion and contraction of TM slabs during cycling. Meanwhile, the successful realization of gradual decreasing in operating voltage strongly validates the effectiveness and tunability of our structural design. (Supplementary Fig. 60)

Overall, this study proposes a structural design strategy for negative electrode materials by integrating intraplanar percolation-interplanar bridging in the layered matrix, which combines the advantages of mainstream battery material structures to develop negative electrode materials for batteries with high capacity/rate capability, long cycling, and zero-strain behavior over a wide-temperature range. Taking the low-cost vanadium-based compound KVO as a representative, the abundant pentagonal tunnels in its active TM layers facilitate rapid intraplanar Li^+ percolation, while the KO_{10} polyhedrons formed by large-radius K^+ between layers act as bridging units, which can not only widen the interlayer spacing to retain sufficient Li^+ intercalation sites, but also effectively constrain the expansion of TM layers, endowing the material with enhanced structural stability. At 30//60// −10 °C, the as-prepared KVO compound displays high capacity of 377//385//184 mAh g^{-1} at 0.1 C, and exhibits rate performance and long-term cyclability with capacity retention of 88.3 % at 10 C rate after 19000 cycles at 30 °C. The in-situ XRD, ex-situ XAS, and other characterizations confirm that V in KVO undergoes a two-electron transfer process ($V^{5+} \leftrightarrow V^{3+}$) during Li^+ (de)lithiation. DFT calculations combined with GITT reveal that the 3D Li^+ diffusion pathways in KVO, ensure fast charging/discharging capability. Most importantly, the complementary volume changes between KO_{10} polyhedrons and the VO_x layers in KVO result in a maximum lattice parameter variation of only 0.11% during cycling, realizing zero-strain characteristics. The universality of this structural design strategy has been also verified by other materials, such as $K_2VP_2O_8$, $K_2MgV_2O_7$, and $Rb_3V_5O_{14}$, all of which exhibit high-capacity/rate capability, long cycling, and zero-strain behavior. In summary, this study has successfully demonstrated a general structural design strategy of high-performance electrode materials for next-generation batteries, while plenty of work is still needed for the commercial application of the as-designed materials in the future.

https://doi.org/10.1038/s41467-026-69387-z

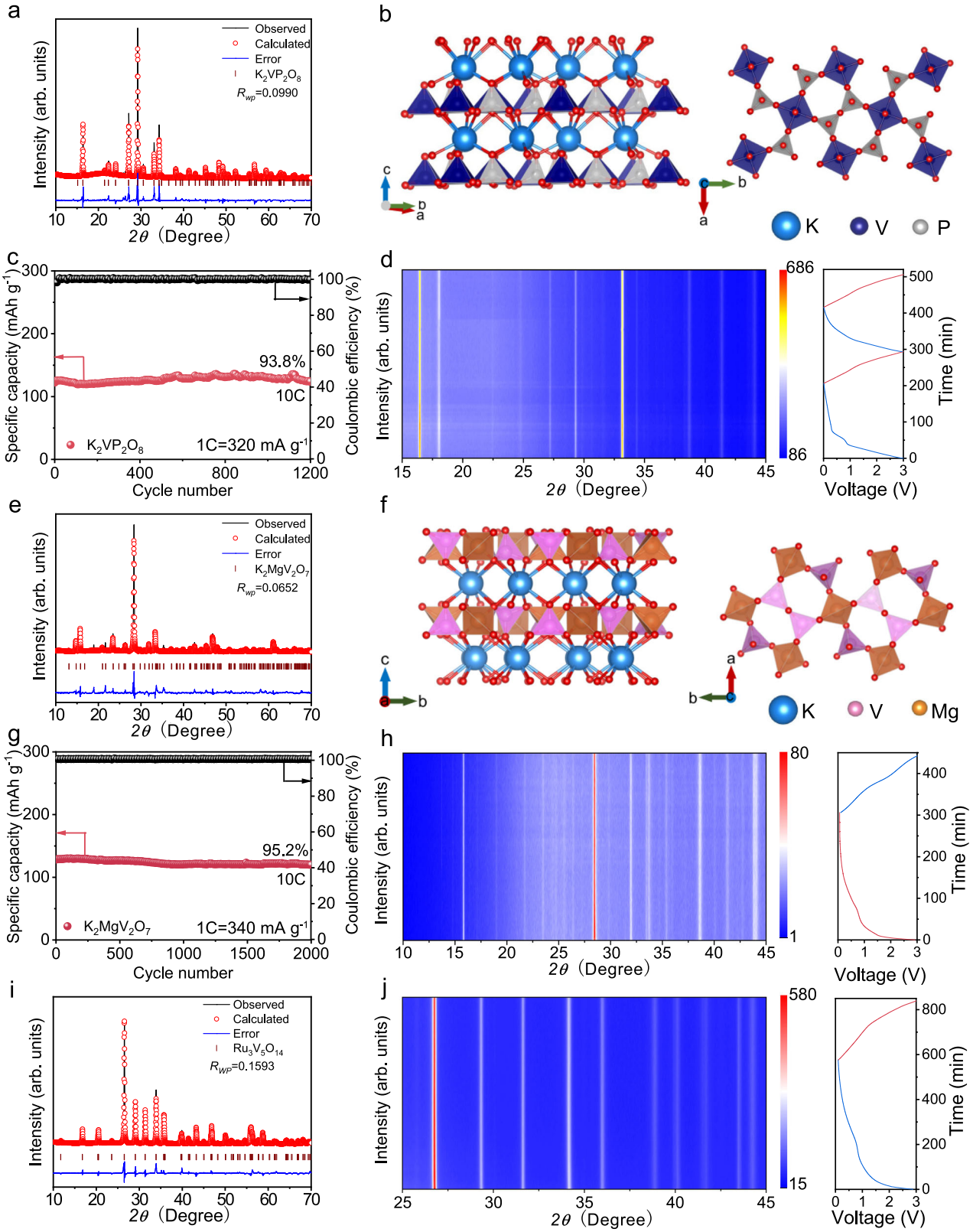

Fig. 6 | Discovery and characterization of other layered structure according to the proposed strategy. XRD pattern with Rietveld refinement (**a**) schematic crystal structure (**b**) electrochemical performance at 30 °C (1 C = 320 mA g^{-1}) (**c**) and in-situ XRD patterns of $K_2VP_2O_8$ at 30 °C (initial two cycles at 0.3 C) (**d**). XRD pattern with Rietveld refinement (**e**), schematic crystal structure (**f**) electrochemical performance at 30 °C (1 C = 340 mA g^{-1}) (**g**) and in-situ XRD patterns of $K_2MgV_2O_7$ at 30 °C (initial cycle at 0.2 C) (**h**). **i**, **j** XRD pattern with Rietveld refinement (**i**), and in-situ XRD patterns of $Rb_3V_5O_{14}$ at 30 °C (initial cycle at 0.2 C,1 C = 342 mA g^{-1}) (**j**).

Methods

Material synthesis

The synthesis of KVO sample was conducted via a straightforward and cost-effective solid-state reaction method. Specifically, NH_4VO_3 (99 %, Macklin) and K_2CO_3 (99 %, Macklin) powders were thoroughly mixed in a molar ratio of 10:3, with the weighed masses of 5.849 g for NH_4VO_3 and 2.073 g for K_2CO_3. Subsequently, the mixture underwent energetic milling using a high-energy ball-milling machine (SPEX 8000 M, SPEX SamplePrep, USA) equipped with an 8007 stainless steel vial (volume: 65 mL). The milling media consisted of two 1/2 in. (12.7 mm) and four 1/4 in. (6.35 mm) stainless steel balls. The milling program was set as follows: continuous operation for 60 min, followed by an intermittent rest time of 30 min, and this cycle was repeated 10 times (total milling duration: 15 h) at a rotational speed of 1725 r min^{-1}. After ball-milling, the resultant powder was collected and subjected to calcination at 400 °C for 8 h in air using a muffle furnace (KSL-1200X-J, Hefei Kejing Material Technology Co., Ltd) with a ramp rate of 5 °C min^{-1}.Similarly, $K_2VP_2O_8$ samples were fabricated through a solid-state reaction route. Initially, NH_4VO_3 (99 %, Macklin), K_2CO_3 (99 %, Macklin), and $NH_4H_2PO_4$ (99.9 %, Macklin) powders were uniformly blended at a molar ratio of 1:1:2, with the weighed amounts of 1.170 g, 1.382 g, and 2.301 g respectively. Subsequently, the mixture underwent high-energy ball milling using the same SPEX 8000 M equipment equipped with an 8007 stainless steel vial, adopting the same milling protocol: 60 min of continuous grinding, 30 min of intermittent rest, and 10 cycles of repetition at 1725 r min^{-1}. Following milling, the obtained powder was gathered and calcined in air at 550 °C for 8 h via a KSL-1200X-J muffle furnace with a heating rate of 5 °C min^{-1}. Micrometer-sized $K_2MgV_2O_7$ particles were prepared via a solid-state reaction protocol. NH_4VO_3 (99 %, Macklin), K_2CO_3 (99 %, Macklin), and MgO (99.9 %, Macklin) were first weighed out as the starting materials (2.340 g, 1.382 g, and 0.403 g respectively) and then mixed homogeneously at a molar ratio of 2:1:1. The mixture was subsequently processed by high-energy ball milling using a SPEX 8000 M apparatus paired with an 8007 stainless steel via. Two 1/2 in. (12.7 mm) and four 1/4 in. (6.35 mm) stainless steel balls served as the milling media, and the milling was carried out following the same procedure as above: 60 min of continuous operation alternating with 30 min of intermittent rest, repeated 10 times (total milling duration: 15 h) at 1725 r min^{-1}. After milling, the powder was collected and calcined in air at 850 °C for 8 h in a KSL-1200X-J muffle furnace with a heating rate of 5 °C min^{-1}. $Rb_3V_5O_{14}$ samples were fabricated via a solid-state reaction method. Firstly, Rb_2CO_3 (99 %, Macklin) and NH_4VO_3 (99 %, Macklin) were weighed as 3.464 g and 5.849 g, respectively, and mixed homogeneously at a molar ratio of 3:10. The mixture was then processed by high-energy ball milling following the same procedure as above. After milling, the powder was collected and calcined in air at 500 °C for 6 h using a KSL-1200X-J muffle furnace with a heating rate of 5 °C min^{-1}.Both commercial graphite (SFC-E) and commercial $LiFePO_4$ (P198) were purchased at Shenzhen BTR New Energy Materials Co., LTD. $Li_4Ti_5O_{12}$ (MA-EN-AN-0020) was purchased at Guangdong Canrd New Energy Technology Co., LTD.

Material characterizations

The KVO crystal structure was characterized via XRD measurements conducted on a Bruker D8 Discover diffractometer equipped with Cu-Kα radiation. The instrument operated at 40 kV and 40 mA in reflection geometry. The XRD patterns underwent Rietveld refinement with the General Structure Analysis System (GSAS) software. Neutron powder diffraction (NPD) data were collected using the Echidna instrument at the Australian Nuclear Science and Technology Organisation (ANSTO). Structural refinements were executed via the Rietveld method, implemented in the GSAS (General Structure Analysis System) software suite. Morphological characteristics were examined using FESEM on an FEI Tecnai G2 F20 STWIN instrument. Additionally, TEM combined with EDS was performed on a Tecnai G2 F20 system. Additionally, ex-situ XPS measurements were performed with a PHI 5000 Versa Probe II system, using monochromatic Al-Kα irradiation at 1486.6 eV.

Electrochemical tests

The four electrodes were fabricated by mixing 80 wt.% active material (KVO, $K_2VP_2O_8$, $K_2MgV_2O_7$ or $Rb_3V_5O_{14}$), 10 wt.% Super-P conductive carbon (99.5%, Canrd Technology Co., Ltd.), and 10 wt.% polyvinylidene fluoride (PVDF, MA-EN-BI-0009, Arkema, molecular weight: ~1,000,000) in N-Methyl-2-pyrrolidinone (NMP, 99.5%, Sigma-Aldrich). The resulting slurry was evenly spread onto copper foils (≥99.8%, 9 μm) using a coating instrument (MSK-AFA-ES200, Shenzhen Kejing Star Technology Co., Ltd.). Active materials ($Li_4Ti_5O_{12}$, graphite or $LiFePO_4$), Super-P conductive carbon and PVDF in a mass ratio of 8:1:1 were mixed in NMP to spread on current collectors using the same coating instrument− copper foils (≥99.8%, 9 μm) for $Li_4Ti_5O_{12}$ or graphite, and aluminum foils (≥99.6%, 16 μm) for $LiFePO_4$.After vacuum drying at 60 °C for 12 hours, the electrodes were further heated to 120 °C for 2 h, and then the resulting electrodes were trimmed into 12 mm diameter circular sheets using an MSK-T10 instrument (Shenzhen Kejing Star Technology Co., Ltd.).

In the argon-filled glove box, half cells were assembled using KVO, $K_2VP_2O_8$, $K_2MgV_2O_7$, $Rb_3V_5O_{14}$, $Li_4Ti_5O_{12}$ or graphite as the working electrode and Li metal (diameter: ~16.0 mm, thickness: ~0.5 mm) as the counter and reference electrode. The average loading of negative electrodes was ~5.0 mg/cm^2. To fabricate pre-lithiated KVO negative electrodes used in KVO||$LiFePO_4$ full cells, Li||KVO half cells were subjected to one cycle at 0.1 C within a voltage range of 0.2–3 V prior to disassembly in an argon-atmosphere glove box. The positive electrodes in full cells utilized commercial $LiFePO_4$ with an N/P ratio of ~1.05 (the average loading of $LiFePO_4$ is ~12.5 mg/cm^2). The current rate of 1 C for both half and full cells was equal to 450 mA g^{-1}, corresponding to the theoretical capacity of KVO. Their specific capacities were calculated based on the mass of KVO on the working electrodes. Similarly, $Li_4Ti_5O_{12}$||$LiFePO_4$ full cells were assembled using commercial $LiFePO_4$ for the positive electrodes and commercial $Li_4Ti_5O_{12}$ for the negative electrodes (an N/P ratio of ~1.05, 1 C = 175 mA g^{-1} for $Li_4Ti_5O_{12}$). All half and full cells was fabricated in the 2032-type coin cell. The electrolyte consisted of 1 M $LiPF_6$ dissolved in an equal-volume mixture of ethylene carbonate, diethyl carbonate, and dimethyl carbonate (LB315, Zhangjiagang Guotai Huarong New Chemical Materials Co., Ltd.). The electrolyte for all coin cells was controlled at 80 μL. As separators, microporous polypropylene films (Celgard® 2325, thickness: 25 μm, Gurley value: 620 s, porosity: 39%, one piece per cell, Canrd Technology Co., Ltd.) were utilized. Galvanostatic charge/discharge tests and GITT studies were conducted using a multichannel battery tester from Wuhan Land Electronic Co., Ltd., China. Electrochemical impedance spectroscopy (EIS) tests and CV tests were performed using a CHI 660E electrochemical workstation. The EIS measurements were conducted under a potentiostatic mode with an alternating current (AC) signal amplitude of 5 mV. The frequency range was set from 10^5 Hz to 10^{-1} Hz, with 73 total data points for sufficient spectral resolution. after target cycles, all cells stood for 30 min to eliminate galvanostatic-induced concentration polarization and bring electrode-electrolyte interface to quasi-stationary state, ensuring reliable EIS data. All ex-situ measurements were performed following the procedure below: all cycled electrodes were promptly collected from the cells at designated voltages to mitigate side reactions between the cycled electrodes and electrolyte. Subsequently, the electrodes were thoroughly rinsed with dimethyl carbonate to eliminate soluble surface species. After drying, all electrodes were transferred into the experimental vacuum chamber via a custom-designed sample transfer module in an argon-filled glove box, ensuring no exposure to ambient air. All electrochemical tests were conducted in

climatic chambers at different temperatures, including: 30 °C and 60 °C climatic chambers (SPX-150BIII, temperature fluctuation: ±0.5 °C, Tianjin Taiste Instrument Co., Ltd.) and −10 °C low-temperature climatic chamber (ECT-150-70 CP SD, temperature fluctuation: ±0.2 °C, Giant Force Instrument Enterprise Co., Ltd.).

In-situ characterizations

To investigate the crystal-structural evolution, in-situ half-cells were assembled for XRD analysis using a LIB-LHTXRD-LN system (Beijing Scistar Technology Co., Ltd.). Each cell was configured with a fiberglass separator and a beryllium window, enabling in-situ XRD measurements. The Rietveld refinement of the XRD pattern was performed by using the GSAS software with the EXPGUI interface. For real-time observation of morphological and structural evolution, in-situ TEM was employed. This was facilitated by an electrochemical holder developed by the X-mech Center at Zhejiang University. In the in-situ TEM half cell, the two electrodes consisted of KVO particles on a silver rod and lithium metal on a tungsten rod, respectively. A Li_2O coating, acting as a solid electrolyte, formed on the surface of the lithium metal. Lithiation processes, transitioning from lithium metal to Li_2O and further to KVO, were induced by applying a negative voltage of −3.0 V when the two electrodes were in contact.

Related characterization of synchrotron radiation

Soft XAS experiments were performed at the V L-edge, O K-edge, and F K-edge using beamline 02B02 at the Shanghai Synchrotron Radiation Facility (SSRF). Photons ranging from 50 to 2000 eV were provided by the bending magnetic beamline, with a sample beam size of 150 μm × 50 μm. Spectra for V, O, and F were simultaneously collected using surface-sensitive TEY and TFY modes. Beam energy calibration was carried out using the spectra of $SiTiO_3$ and LiF samples. The bulk chemical evolution was investigated by hard XAS at the SSRF Beamline 1W1B. Additionally, V_2O_5, VO_2 and $C_{15}H_{21}O_6V$ were utilized as standard samples for V^{5+}, $V^{4+}$and V^{3+}, respectively.

Theoretical calculations

To elucidate the Li^+-storage mechanisms and determine structural energetics, DFT calculations[60] were implemented with the Vienna Ab-initio Simulation Package (VASP). Structural optimization employed the projector augmented wave (PAW) approach[61] together with the Perdew–Burke–Ernzerhof (PBE) functional under the generalized gradient approximation[62]. A simplified grid model (1 × 1 × 1) of KVO served as the initial framework. The plane-wave basis set was defined by a cutoff energy of 400 eV, while convergence thresholds were set at 10^{-6} eV for total energy and 0.005 eV $Å^{-1}$ for atomic forces.

Data availability

All relevant data that support the findings of this study are presented in the manuscript and supplementary information file. Source data are provided with this paper.

References

1. Liu, H. et al. A disordered rock salt anode for fast-charging lithium-ion batteries. *Nature* **585**, 63–67 (2020).
2. Larcher, D. & Tarascon, J. M. Towards greener and more sustainable batteries for electrical energy storage. *Nat. Chem.* **7**, 19–29 (2015).
3. Bi, Y. et al. Reversible planar gliding and microcracking in a single-crystalline Ni-rich cathode. *Science* **370**, 1313–1317 (2020).
4. Sun, H. et al. Three-dimensional holey-graphene/niobia composite architectures for ultrahigh-rate energy storage. *Science* **356**, 599–603 (2017).
5. Obrovac, M. N. & Chevrier, V. L. Alloy negative electrodes for Li-ion batteries. *Chem. Rev.* **114**, 11444–11492 (2014).
6. Etacheri, V. et al. Challenges in the development of advanced Li-ion batteries: a review. *Energy Environ. Sci.* **4**, 3243–3262 (2011).
7. Poizot, P. et al. Nano-sized transition-metal oxides as negative-electrode materials for lithium-ion batteries. *Nature* **407**, 496–499 (2000).
8. Saubanère, M. et al. The intriguing question of anionic redox in high-energy density cathodes for Li-ion batteries. *Energy Environ. Sci.* **9**, 984–1000 (2016).
9. Sathiya, M. et al. Reversible anionic redox chemistry in high-capacity layered-oxide electrodes. *Nat. Mater.* **12**, 827–834 (2013).
10. Yabuuchi, N. et al. Detailed studies of a high-capacity electrode material for rechargeable batteries, Li_2MnO_3–$LiCo_{1/3}Ni_{1/3}Mn_{1/3}O_2$. *J. Am. Chem. Soc.* **133**, 4404–4407 (2011).
11. McCalla, E. et al. Visualization of O-O peroxo-like dimers in high-capacity layered oxides for Li-ion batteries. *Science* **350**, 1516–1520 (2015).
12. Zhang, W. et al. High-rate, Kinetic pathways of ionic transport in fast-charging lithium titanate. *Science* **367**, 1030–1034 (2020).
13. Zhao, B. et al. Facile Synthesis of a 3D nanoarchitectured $Li_4Ti_5O_{12}$ electrode for ultrafast energy storage. *Adv. Energy Mater.* **6**, 1500924 (2016).
14. Deng, S. et al. Boosting fast energy storage by synergistic engineering of carbon and deficiency. *Nat. Commun.* **11**, 132 (2020).
15. Yang, Y. et al. Achieving ultrahigh-rate and high-safety Li^+ storage based on interconnected tunnel structure in micro-size niobium tungsten oxides. *Adv. Mater.* **32**, 1905295 (2020).
16. Lv, C. et al. Rational design and synthesis of nickel niobium oxide with high-rate capability and cycling stability in a wide temperature range. *Adv. Energy Mater.* **12**, 2102550 (2022).
17. Su, F. et al. A high-performance rocking-chair lithium-ion battery-supercapacitor hybrid device boosted by doubly matched capacity and kinetics of the faradaic electrodes. *Energy Environ. Sci.* **14**, 2269–2277 (2021).
18. Griffith, K. J. et al. Niobium tungsten oxides for high-rate lithium-ion energy storage. *Nature* **559**, 556–560 (2018).
19. Yao, W. et al. Structural insights into the lithium-ion storage behaviors of niobium tungsten double oxides. *Chem. Mater.* **34**, 388–396 (2022).
20. Li, T. et al. A niobium oxide with a shear structure and planar defects for high-power lithium-ion batteries. *Energy Environ. Sci.* **15**, 254–262 (2022).
21. Zhang, Y. et al. Delocalized electronic engineering of $TiNb_2O_7$ enables low temperature capability for high-areal-capacity lithium-ion batteries. *Nat. Commun.* **15**, 6299 (2024).
22. Liang, G. et al. Conductive $Li_{3.08}Cr_{0.02}Si_{0.09}V_{0.9}O_4$ anode material: novel "zero-strain" characteristic and superior electrochemical Li^+ storage. *Adv. Energy Mater.* **10**, 1904267 (2020).
23. Li, H. et al. Li_3VO_4: a promising insertion anode material for lithium-ion batteries. *Adv. Energy Mater.* **3**, 428–433 (2013).
24. Yang, L. et al. A new sodium calcium cyclotetravanadate framework: "zero-strain" during large-capacity lithium intercalation. *Adv. Funct. Mater.* **32**, 2105026 (2022).
25. Wang, W. et al. Conductive $LaCeNb_6O_{18}$ with a very open A-site-cation-deficient perovskite structure: a fast- and stable-charging Li^+-storage anode compound in a wide temperature range. *Adv. Energy Mater.* **12**, 2200656 (2022).
26. Li, X. et al. Perovskite-type $SrVO_3$ as high-performance anode materials for lithium-ion batteries. *Adv. Mater.* **34**, 2107262 (2021).
27. Ette, P. M. et al. Ordered 1D and 3D mesoporous Co_3O_4 structures: effect of morphology on Li-ion storage and high rate performance. *Electrochim. Acta* **310**, 184–194 (2019).
28. Su, L. et al. Ultrathin layered hydroxide cobalt acetate nanoplates face-to-face anchored to graphene nanosheets for high-efficiency lithium storage. *Adv. Funct. Mater.* **27**, 1605544 (2017).
29. Liu, Y. et al. Lithium-ion storage in lithium titanium germanate. *Nano Energy* **66**, 104094 (2019).

30. Thackeray, M. M. & Amine, K. $Li_4Ti_5O_{12}$ spinel anodes. *Nat. Energy* **6**, 683–695 (2021).
31. Li, G.-X. et al. Enhancing lithium-metal battery longevity through minimized coordinating diluent. *Nat. Energy* **9**, 817–827 (2024).
32. Yan, B. et al. An elaborate insight of lithiation behavior of V_2O_5 anode. *Nano Energy* **78**, 105233 (2020).
33. Liao, C. et al. Si-doping mediated phase control from *β*- to *γ*-form Li_3VO_4 toward smoothing Li insertion/extraction. *Adv. Energy Mater.* **8**, 1701621 (2018).
34. Armstrong, A. R. et al. The lithium intercalation process in the low-voltage lithium battery anode $Li_{1+x}V_{1-x}O_2$. *Nat. Mater.* **10**, 223–229 (2011).
35. Wu, H. et al. Stable Li-ion battery anodes by in situ polymerization of conducting hydrogel to conformally coat silicon nanoparticles. *Nat. Commun.* **4**, 1943 (2013).
36. Liu, P. et al. Hierarchical porous intercalation-type V_2O_3 as high-performance anode materials for Li-ion batteries. *Chem. Eur. J.* **23**, 7538–7544 (2017).
37. Mansour, A. N. et al. A comparative in situ X-ray absorption spectroscopy study of nanophase V_2O_5 aerogel and ambigel cathodes. *J. Electrochem. Soc.* **150**, A403–A408 (2003).
38. Mansour, A. N. et al. In situ X-ray absorption spectroscopy characterization of V_2O_5 xerogel cathodes upon lithium intercalation. *J. Electrochem. Soc.* **146**, 2387–2392 (1999).
39. Zhang, L. et al. Lithium lanthanum titanate perovskite as an anode for lithium-ion batteries. *Nat. Commun.* **11**, 3490 (2020).
40. Lu, X. et al. Atomic-scale investigation on lithium storage mechanism in $TiNb_2O_7$. *Energy Environ. Sci.* **4**, 2638–2645 (2011).
41. Zhang, F. et al. Boosting charge carrier transport by layer-stacked $Mn_xV_2O_6/V_2C$ heterostructures for wide-temperature zinc-ion batteries. *Adv. Funct. Mater.* **34**, 2402071 (2024).
42. Wang, A. et al. Building stabilized $Cu_{0.17}Mn_{0.03}V_2O_5$–$2.16H_2O$ cathode enables an outstanding room-/low-temperature aqueous Zn-ion batteries. *Carbon Energy* **6**, e512 (2024).
43. Ding, J. et al. In situ lattice tunnel distortion of vanadium trioxide for enhancing zinc ion storage. *Adv. Energy Mater.* **11**, 2100973 (2021).
44. Zhao, D. et al. Unlocking the capacity of vanadium oxide by atomically thin graphene-analogous $V_2O_5{\cdot}nH_2O$ in aqueous zinc-ion batteries. *Adv. Funct. Mater.* **33**, 2211412 (2023).
45. Zhang, Q. et al. A multi-colored, structure-tolerant vanadate cathode for high-performance aqueous zinc-ion batteries. *Adv. Energy Mater.* **15**, 2404597 (2025).
46. Jayaraman, S. et al. Exceptional performance of $TiNb_2O_7$ anode in all one-dimensional architecture by electrospinning. *ACS Appl. Mater. Interfaces* **6**, 8660–8666 (2014).
47. Ma, S. et al. VPO_5: an all-climate lithium-storage material. *Energy Storage Mater.* **46**, 366 (2022).
48. Cui, Y. et al. Silicon anodes. *Nat. Energy* **6**, 995–996 (2021).
49. Huo, H. et al. Chemo-mechanical failure mechanisms of the silicon anode in solid-state batteries. *Nat. Mater.* **23**, 543–551 (2024).
50. Zuo, W. et al. Microstrain screening towards defect-less layered transition metal oxide cathodes. *Nat. Nanotechnol.* **19**, 1644–1653 (2024).
51. Jousseaume, T. et al. Strain and collapse during lithiation of layered transition metal oxides: a unified picture. *Energy Environ. Sci.* **17**, 2753 (2024).
52. Ma, L. et al. Stabilizing the bulk-phase and solid electrolyte interphase of silicon microparticle anode by constructing gradient-hierarchically ordered conductive networks. *Adv. Mater.* **36**, 2404360 (2024).
53. Kühne, M. et al. Reversible superdense ordering of lithium between two graphene sheets. *Nature* **564**, 234–238 (2018).
54. Zhang, L. et al. Lithium whisker growth and stress generation in an in situ atomic force microscope–environmental transmission electron microscope set-up. *Nat. Nanotechnol.* **15**, 94–99 (2020).
55. Zhou, Y.-N. et al. Tuning charge–discharge induced unit cell breathing in layer-structured cathode materials for lithium-ion batteries. *Nat. Commun.* **5**, 5381 (2014).
56. Toby, B. EXPGUI, a graphical user interface for GSAS. *J. Appl. Crystallogr.* **34**, 210–213 (2001).
57. Ravel, B., Newville, M. & Athena, A. rtemis Hephaestus: data analysis for X-ray absorption spectroscopy using IFEFFIT. *J. Synchrotron Radiat.* **12**, 537–541 (2005).
58. Chen, J. et al. Wood-inspired anisotropic hydrogel electrolyte with large modulus and low tortuosity realizing durable dendrite-free zinc-ion batteries. *Proc. Natl. Acad. Sci. USA* **121**, e2322944121 (2024).
59. Zhang, Q. et al. Zero-strain" $K_2SrV_4O_{12}$ as a high-temperature friendly Li^+-storage material. *Energy Storage Mater.* **52**, 637–645 (2022).
60. Blochl, P. E. Projector augmented-wave method. *Phys. Rev. B* **50**, 17953–17979 (1994).
61. Perdew, J. P. et al. Generalized gradient approximation made simple. *Phys. Rev. Lett.* **77**, 3865–3868 (1996).
62. Kresse, G. & Furthmuüller, J. Efficient iterative schemes for ab initio total-energy calculations using a plane-wave basis set. *Phys. Rev. B* **54**, 11169–11186 (1996).

Acknowledgements

This work was supported by The Key R&D Program of Heilongjiang province (2023ZX04A01 to N.L.), The National Key R&D Program of China (2021YFC2902905 to N.L.), The Key Project of Chongqing Technology Innovation and Application Development (2022TIAD-DEX0024 to N.L., 2023TIAD-KPX0007 to N.L.), Beijing Nova Program, Chongqing Outstanding Youth Fund (2022NSCQ-JQX3895 to N.L.), National Natural Science Foundation of China (22109010 to N.L.). The authors thank Shanghai Synchrotron Radiation Facility (SSRF) (beamline BL02B02) and Beijing Synchrotron Radiation Facility (BSRF) (beamline 1W1B) for the allocation of synchrotron beam time.

Author contributions

N.L. proposed and supervised the project. S.M. and W.Y. contributed equally to this work. S.M. carried out the experiments and data analysis. W.Y. conducted electrochemical performance tests. S.W., X.S. and Y.D. conducted in-situ XRD and analysis. X.Z., T.L. and Y.Z. assisted in revising the work. L.C., Q.H., M.W. and Y.G. performed in-situ TEM, XAS and data analysis. W.K. conducted ND and analysis. S.M., Y.S., F.W. and N.L. wrote and revised the manuscript, and all the authors discussed and commented on the manuscript.

Competing interests

The authors declare no competing interests.

Additional information

Supplementary information The online version contains supplementary material available at https://doi.org/10.1038/s41467-026-69387-z.

Correspondence and requests for materials should be addressed to Yuefeng Su or Ning Li.

Peer review information *Nature Communications* thanks Yoojin Ahn, and the other, anonymous, reviewer(s) for their contribution to the peer review of this work. A peer review file is available.